



# Development of a Micro Temperature Sensor and 3D Temperature Analysis for a Proton Exchange Membrane Fuel Cell

H. Y. Wang<sup>1</sup>, W. J. Yang<sup>1</sup>, D. W. Lee<sup>1</sup>, Y. B. Kim<sup>1\*</sup>

<sup>1</sup> Department of Mechanical Engineering, Chonnam National University, Gwangju, Republic of Korea

Received September 12, 2013; accepted April 09, 2014; published online June 17, 2014

## Abstract

This study examines the development of micro *in situ* sensors and analyzed the through-plane temperature of a fuel cell. Temperature sensing inside a fuel cell is important in fuel cell diagnosis and analysis. Temperature sensors must be adequately small, so that fuel cell performance is maintained and the temperature anywhere inside the cell can be flexibly measured. In this study, a temperature sensor based on a micro-electromechanical system (MEMS) is designed and fabricated to achieve these objectives. The micro temperature sensor was installed inside a cell to measure through-plane temperature. The current and voltage of the fuel cell with the micro temperature sensor were measured and compared with those of a fuel cell without the sensor to analyze the effect of the sensor on fuel cell performance. The

developed temperature sensor is of resistance temperature detector (RTD) type, with a flexible substrate of polyimide, high sensitivity, and easy installation characteristics. After calibration of the sensors, three sensors were inserted into the cell to measure the through-plane temperature, and the polarization curve of the cell with and without the micro sensor was compared. Finally, a 3D computational fluid dynamics (CFD) model of a fuel cell was developed and analyzed by comparison of the measured temperature results to determine the accuracy of the model.

**Keywords:** Computational Fluid Dynamic Analysis, Computational Fluid Dynamics Validation, Micro Sensor, Temperature Measurement, Temperature Sensor

## 1 Introduction

The performance of a proton exchange membrane fuel cell (PEMFC) is significantly affected by operating parameters, such as gas stoichiometry, temperature, and relative humidity [1]. Analyzing these operating parameters is indispensable to improve PEMFC operation and enhance fuel cell performance. Most researchers have attempted to accurately measure these parameters with several instruments and methods. Fuel cell hybrid vehicles, such as Tucson IX of Hyundai Motors in Korea, are now on the market [2]. Therefore, the sensing technique is important to improve not only performance but also fuel cell life. Temperature is an important parameter that is closely associated with the criterion for fuel cell performance. Determining the temperature distribution inside a fuel cell is important to monitor the performance of the cell and extend its life.

Many researchers have measured the distribution and temperature of fuel cell species with commercial external sensors. For instance, Hinds et al. [3] used commercial SHT75 temperature/humidity sensors to measure the temperature

on a straight PEMFC. They designed a bipolar plate to insert the sensors at six locations along the channel by bypassing the vapor. The sensors can measure the temperature in real time, but special machining is necessary to insert the sensors; bypassing the vapor renders this type of measurement complex and inaccurate. Partridge et al. [4] used spatially resolved capillary-inlet mass spectrometry to measure species distribution inside a fuel cell. They successfully analyzed transient oxygen and hydrogen consumptions with load variation, but their measuring device is bulky, expensive, and difficult to use. Chen et al. [5] used neutron radiography to measure species distribution. They utilized a shifted anode and cathode channel to identify the water transport mechanism of each channel. They confirmed the water transport mechanism by comparing simulation and experimental results. However, their measuring facility is extremely complicated and cannot be used real time. Mench et al. [6] used gas chromatography to measure the internal gas species and

[\*] Corresponding author, ybkim@jnu.ac.kr

temperature distributions inside a cell. However, the measuring facility is expensive, and analyzing gas distribution is time consuming. Holes should also be drilled to extract the gases for measurement, and this can cause fuel cell leakage.

Some researchers have measured the fuel cell parameters inside a cell. He et al. [7] designed a special thin film temperature sensor for the real-time measurement of electrolyte temperature in a PEMFC. They used two Nafion 112 films as a membrane, with a thin Parlyen film on Cr/Au electrode in between, to measure internal cell temperature. This technique is novel; however, the sensor can block proton transfer from the anode to the cathode and thus degrade cell performance because the area of the temperature sensor is the same as the membrane area and two membranes are used. Moreover, these two membranes may not provide the real temperature distribution in the fuel cell. Zhang et al. [8] used commercial sensors to measure the internal current and temperature of a cell. They studied the effects of variations in inlet gas flow rate and operating voltage on fuel cell performance. However, their measurement equipment is bulky, and a special current collector design is necessary. Lee et al. [9,10] developed a microelectromechanical (MEMS)-based temperature and voltage sensor to measure temperature and overpotential distributions. Their idea is new and impressive; however, the sensor blocks the diffusion of gases, so cell performance decreases, and real sensed values are difficult to obtain.

Most temperature analyses by numerical method have been performed with the use of lumped model or computational fluid dynamics (CFD) without experimental validation. Shan and Choe [11], Mehekar et al. [12], Xue et al. [13], M. Khandelwal et al. [14], and Wang and Kim [15] developed a lumped model with Matlab or an in-house program to analyze temperature distribution. Meanwhile, many researchers have used the CFD model to examine temperature. For example, Ju et al. [16], Matamoros and Brüggermann [17], Manso et al. [18], Yang et al. [19], and Pharoah and Burheim [20] developed a 2D or 3D CFD model to analyze and discuss temperature distribution. However, none of these researchers compared the temperature distribution with experimental results. Only the polarization curve was compared to validate the CFD model because measuring the internal temperature distribution without micro temperature sensors is difficult.

A new micro temperature sensor was designed and fabricated in this study to address the aforementioned limitations. The developed sensor was built with MEMS technologies by simple MEMS fabrication. Three sensors were used to measure the through-plane temperature distribution of the cell. A single cell with an area of 25 cm<sup>2</sup> was utilized to identify the effect of the sensors on fuel cell performance. The cell has a serpentine flow channel type, and counter-flow was used to obtain the polarization curve. A 3D CFD model was also developed and analyzed to increase the accuracy of numerical analysis by comparison of the temperature distribution between numerical and experimental results.

## 2 Micro Temperature Sensor

MEMS-based sensors are known to have the following advantages in measuring fuel cell species distribution [10]. First, MEMS-based sensors are small enough to be placed anywhere to measure the required values. Second, they provide a real-time sensing signal. MEMS-based sensors also need to be tough but flexible to endure harsh environments because of considerable variations in temperature and pressure inside a cell. If a sensor is too rigid, it can break down during long-term use because the membrane constantly vibrates as a result of the difference in pressure between anode and cathode gases. Furthermore, MEMS-based sensors should be sufficiently thin to avoid gas leakage when they are assembled within a cell. They also require contaminant-free characteristics because of the presence of other gases, such as mono carbon oxide or dioxide. In this regard, a new MEMS sensor based on a polyimide film was developed to meet these requirements. Polyimide film has the following merits: it is tough but flexible; it withstands harmful gas contamination; other metals, such as Au and Cr, can be easily deposited for an electrode [21]; and it can detect humidity for subsequent usage.

Figure 1 shows the fabrication process of the polyimide-based micro-temperature sensor. A 40  $\mu\text{m}$ -thick polyimide film was attached to a silicon wafer. The process begins with the evaporation of a layer of chromium (Cr) on the silicon wafer as a sacrificial layer and the deposition of a 20  $\mu\text{m}$ -thick thin polyimide film as a substrate and sensing material. Afterward, Cr (100 Å) and Au (1,000 Å) were deposited on the polyimide substrate with an e-beam evaporator. Positive PR (AZ4620) coating was applied with soft baking at 95 °C for 90 s. The first lithographic process was applied to define the pattern of the micro-temperature sensor. In this stage, hard baking at 150 °C for 90 s was conducted. The structure of the sensor and the contact pads were formed during the liftoff. Then, another lithographic process was implemented to define the insulation pattern. SU-8 (10  $\mu\text{m}$  thick) was used as the insulation material. Small circles (with a diameter of 2.5  $\mu\text{m}$  and a height of 10  $\mu\text{m}$ ) were created after the second liftoff to minimize the insulation area. Figure 2 shows an enlarged picture of the fabricated temperature sensor.

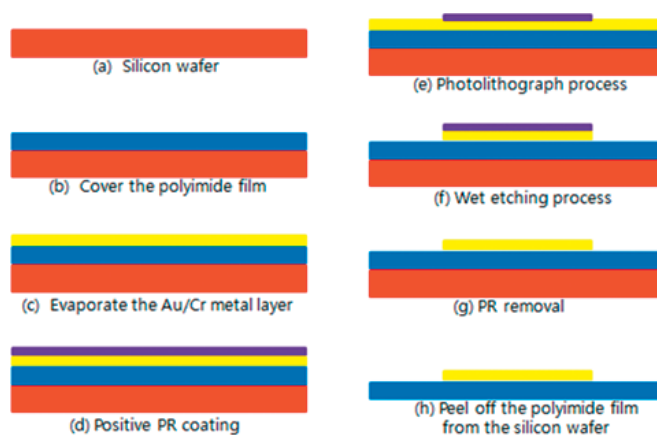


Fig. 1 Fabrication process of a micro temperature sensor.

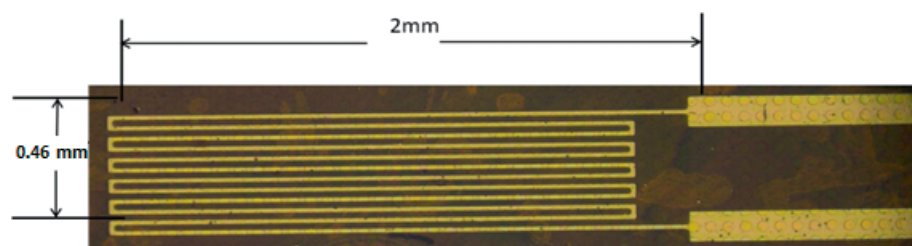


Fig. 2 Enlarged photo of a fabricated temperature sensor (circular pattern shows the insulation layer).

## 3 Results of Sensor Measurement

Sensor properties were analyzed before the micro sensors were used to measure temperature. An accurately controlled temperature chamber was used to determine the accuracy of the sensor. SJ-TH-S50 of SJ Science Company, Korea was used as the temperature test chamber. Figure 3 shows

the properties of each sensor. The temperature sensors show good linearity depending on the temperature variation. Figure 4 shows that three sensors were attached at three points to measure the thorough-plane temperature. Sensor 1 was located between the cathodic gas diffusion layer (GDL) and bipolar plate, sensor 2 was between the cathode membrane electrode assembly (MEA) and GDL, and sensor 3 was between the anodic GDL (GDL) and bipolar plate. All sensors were assembled with MEA, GDL, and bipolar plate; enough pressure was applied to avoid gas leakage. Figure 5 shows the assembly of the temperature sensors. They were constructed at the edge of the cell to minimize interruption to gas diffusion and electron conduction, which degrade fuel cell performance. The dimension of the micro temperature sensor is  $460\text{ }\mu\text{m} \times 1,800\text{ }\mu\text{m}$ , and its thickness is  $40\text{ }\mu\text{m}$ . The

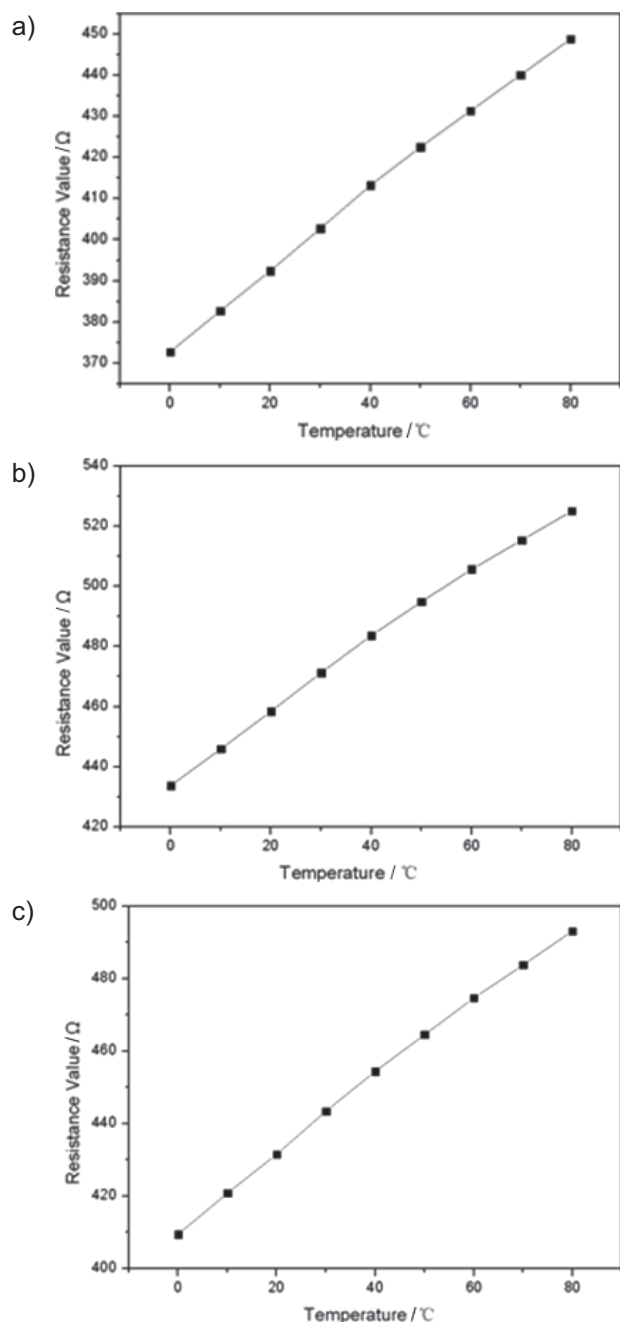


Fig. 3 Calibration curves for three different temperature sensors: (a) front view; (b) side view.

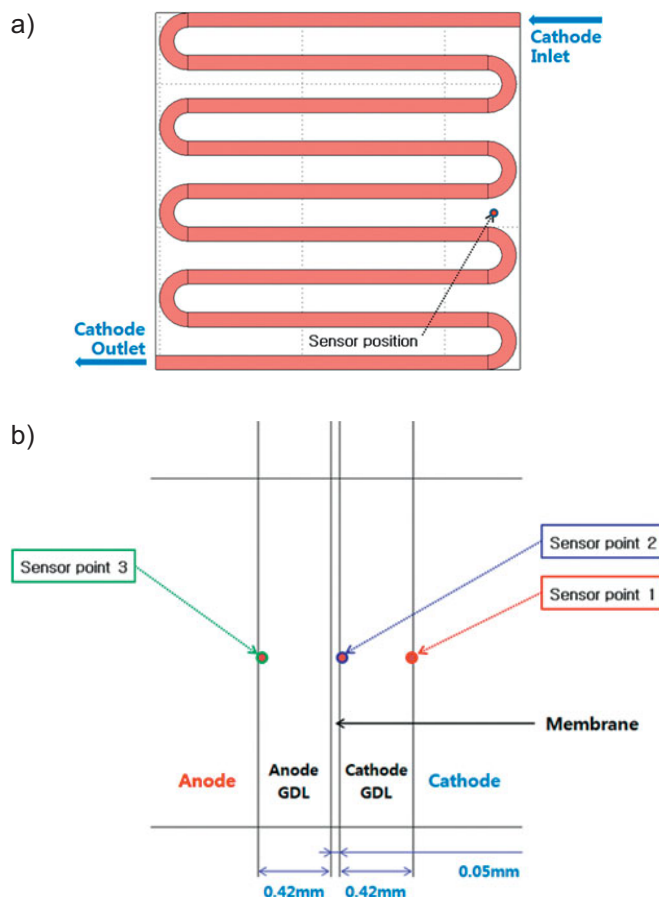


Fig. 4 Location of three sensors.



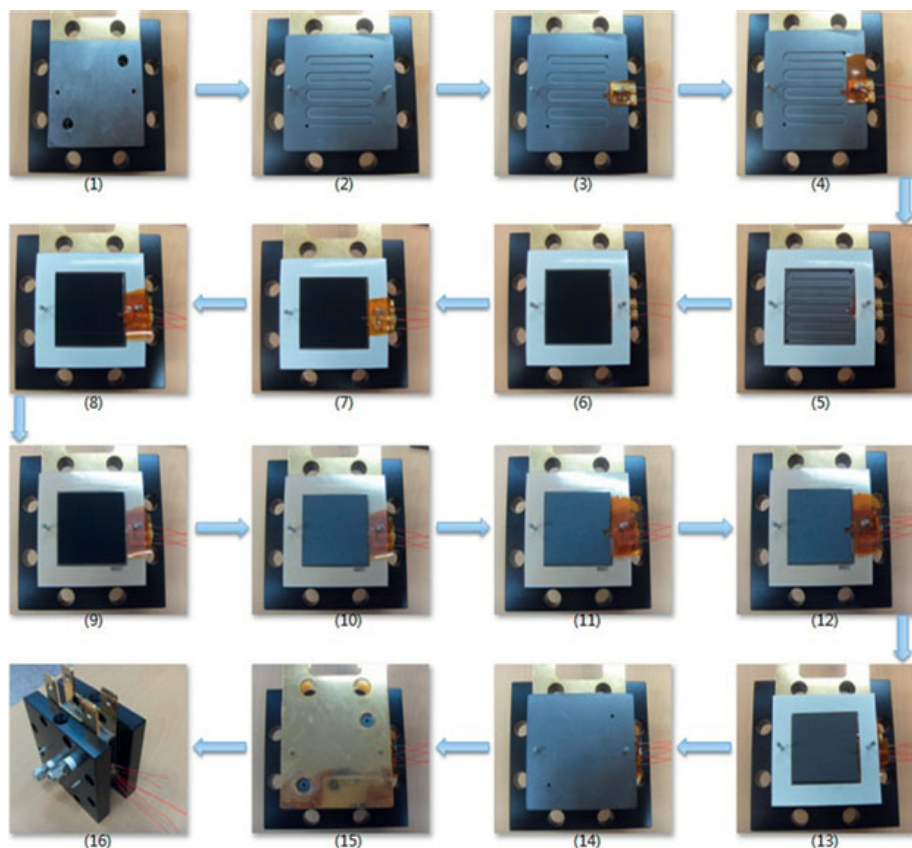


Fig. 5 Assembly process for three sensors. Each figure represents: the first sensor insertion (1–4); cathode gasket and GDL assembly (5–6); the second sensor insertion (7–8); MEA and anode GDL assembly (9–10); the third sensor insertion (11–12); anode gasket with bipolar plate assembly (13–16).

active area of the MEA is  $25 \text{ cm}^2$ , so the sensor interference to block gas diffusion and electron transfer is small.

The effect of the micro-sensor on PEMFC performance was studied by inspection of polarization curves. The conditions in this case were as follows:  $300 \text{ mL min}^{-1}$  anode flow rate,  $1,000 \text{ mL min}^{-1}$  cathode flow rate,  $40^\circ \text{C}$  stack temperature, 100% humidity, 1.5 anode stoichiometry, and 2.0 cathode stoichiometry. Lee et al. [9] reported that micro sensors block gas diffusion and thus eventually degrade the performance of the

fuel cell. More than 50% of performance degradation was observed. Meanwhile, He et al. [7] used micro temperature sensors located between membranes to measure temperature; doing so inherently blocks proton transfer and thus renders real measurement impossible. The MEA of the fuel cell was assembled with a  $100 \text{ }\mu\text{m}$ -thick Gore® membrane and a  $10 \text{ }\mu\text{m}$ -thick catalyst layer sprayed on the membrane with an airbrush. The catalyst was prepared with E-TEK® 40% wt% carbon-supported platinum (Pt) and Nafion® 5 wt% solution. The Pt loading was  $0.3 \text{ mg cm}^{-2}$ . The GDL used was E-TEK® with a  $400 \text{ }\mu\text{m}$ -thick carbon cloth. The bipolar plate had a serpentine flow field; this plate was 1, 2, and 100 mm in depth, width, and length, respectively. The channel had six bends, and a counter-flow channel was used. The fuel cell test station from CNL, Korea was used, and it was equipped with two membrane fuel cells to regulate flow rate and stoichiometry and to adjust temperature and inlet humidity. A heater was installed at the bipolar section to maintain the cell temperature at a certain level. A programmable electrical loader from BP Solutions of Korea was used for the external loading. Figure 6 shows the fuel cell station utilized in the experiment. Figure 7 depicts the comparison of the V-I curves of the fuel cell; three lines, red, blue, and cyan lines, represent the curves with a sensor attached, and the black line is the curve without a sensor. Inserting the temperature sensor had little effect on fuel cell performance. For

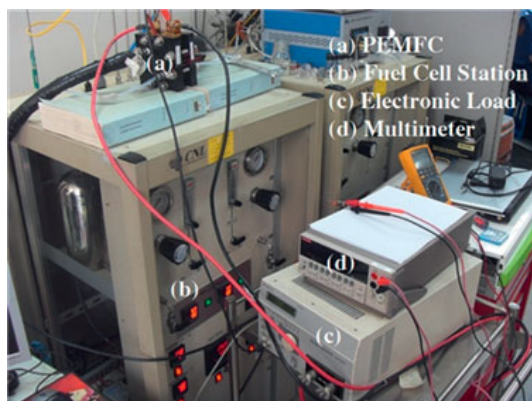


Fig. 6 Fuel cell testing equipment and a fuel cell with micro temperature sensors installed.

able electrical loader from BP Solutions of Korea was used for the external loading. Figure 6 shows the fuel cell station utilized in the experiment. Figure 7 depicts the comparison of the V-I curves of the fuel cell; three lines, red, blue, and cyan lines, represent the curves with a sensor attached, and the black line is the curve without a sensor. Inserting the temperature sensor had little effect on fuel cell performance. For

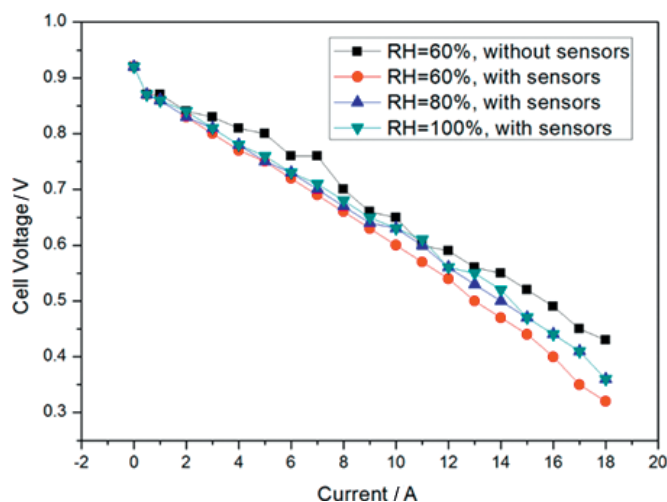


Fig. 7 Performance curve of a single cell with and without sensor.

0.45 V of cell voltage, 16.7% performance degradation was observed with RH = 60%. This performance degradation is an excellent result compared with previous research results, such as the almost 50% degradation of fuel cell performance with the use of the MEMS sensor [9]. However, the measurement of fuel cell temperature without degradation of fuel cell performance must be improved. Next, the performance variations of anode and cathode inlets were measured through a change in the gas flow RH from 60, 80, and 100%. A high RH increases proton conductivity and current flow because of additional active electrochemical reaction. The result is the same even when the sensors are inserted, and they do not significantly affect fuel cell performance. No flooding occurs, and the sensor insertion only slightly interferes with the passage of gas diffusion. This study aims to develop and apply a micro-sensor to measure the internal temperature of a fuel cell, so dehydration or flooding is not the main topic of this study. Overall, the sensor can accurately measure fuel cell properties despite relative humidity changes.

Figure 8 shows the variation in through-plane temperature at three points with an inlet relative humidity of 60, 80, and 100%. Point 1 is the location between the cathode GDL and bipolar plate, and point 2 is the location between the MEA and GDL, so the temperature difference between GDL is almost 0.5 degree and 1 degree at the mid- and high-operating regions, respectively; this result agrees well with previous research findings [1,11]. However, the temperature at point 3, which is the location between the anode GDL and bipolar plate, was lower than that at points 1 and 2 because hydrogen flow lowered the anode temperature. The anode temperature is usually lower than the cathode one because the thermal conductivity of hydrogen is much higher than that of air. This temperature distribution agrees with that in a previous study [14].

## 4 CFD Analysis

The measured temperature can be used to validate a CFD model. A complete 3D PEMFC model with the same geometry used for the experiments was constructed in this study with Comsol multi-physics. Figure 9 shows that the 3D model was developed to represent the unit cell. The model domain is confined within a five-layer MEA, GDL, proton exchange membrane (PEM) with anodic and cathodic catalyst layers, and GDLc. Both feeds were treated as ideal gases and transported through diffusion and convection. The electrodes were treated as homogeneous porous media with uniform morphological properties, such as porosity and permeability. All gases within each electrode exist as a continuous phase. A total of 0.125 million elements were constructed, and grid independence test was performed in a previous study [22], which concluded that grid dependency is insignificant. Therefore, we disregarded the grid test. A linear solver with direct (PARDISO) method was utilized to obtain the results. The following governing equations were used for the CFD model.

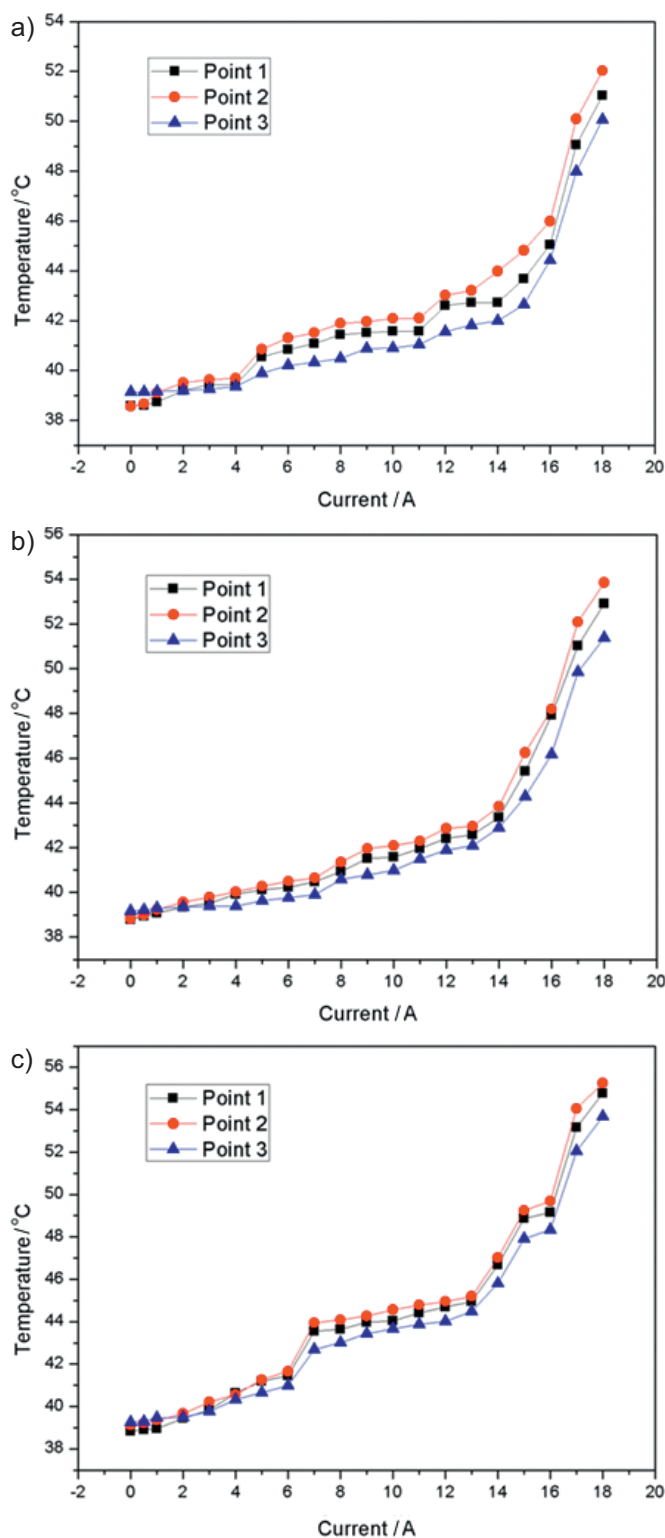


Fig. 8 Temperature variation at three points with the relative humidity variation: (a) RH = 60%; (b) RH = 80%; (c) RH = 100%.

### 4.1 Current Transport

The ionic and electronic current balances in the PEM and GDL are, respectively, described in the following equations

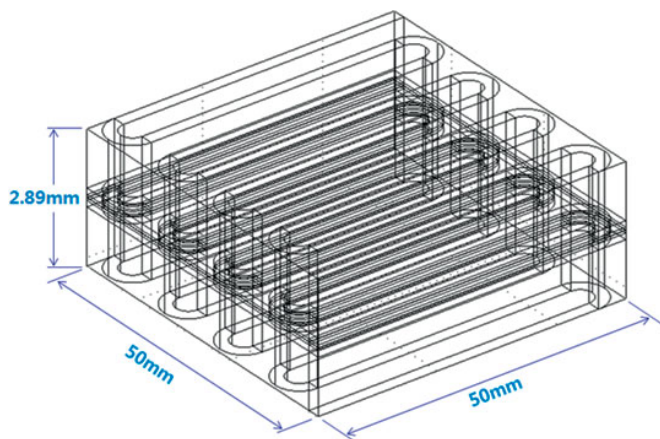


Fig. 9 Geometry of a CFD model.

$$\nabla \cdot i_m = 0 \quad (1)$$

$$\nabla \cdot i_s = 0 \quad (2)$$

where,  $i_s$  and  $i_m$  are the currents flowing through the catalyst and the electrolyte, respectively.

Using Ohm's law, the equations can be represented as

$$\nabla \cdot (-\sigma_m \nabla \phi_m) = 0 \quad (3)$$

$$\nabla \cdot (-\sigma_s \nabla \phi_s) = 0 \quad (4)$$

where,  $\phi_m$  and  $\phi_s$  are the potentials of the ionic conductor (electrolyte) and the electronic conductor (carbon fiber), respectively, and  $\sigma_m$  and  $\sigma_s$  are the ionic and electronic conductivities of the PEM and GDL, respectively.

In the catalyst layer of a PEMFC, the porous matrix contains two kinds of solid phases, i.e. an ionic conductor (electrolyte), and an electronic conductor (catalyst). A potential difference exists between the catalyst and electrolyte to drive the transfer current ( $j_T$ ), keeping the electrochemical reaction continuous. The current passing through the catalyst layer can be decomposed into two parts, i.e.

$$i = i_s + i_m. \quad (5)$$

Because the electrodes are electro-neutral everywhere, there is no charge buildup in the catalyst layers. Thus, the charge conservation is

$$\nabla \cdot i = 0. \quad (6)$$

That is,

$$\nabla \cdot i_s = -\nabla \cdot i_m. \quad (7)$$

These two current components interact through electrochemical reactions. The electrons are transferred to the catalyst from the electrolyte in the anodic catalyst layer, and, similarly, in the cathodic catalyst layer. Application of Ohm's law to the equation yields the current conservation [23].

$$\nabla \cdot (-\sigma_{s,eff} \nabla \phi_s) = -S_c \quad (8)$$

$$\nabla \cdot (-\sigma_{m,eff} \nabla \phi_m) = S_c \quad (9)$$

where, the source terms  $S_c$  and  $-S_c$  are the local transfer current densities corresponding to the hydrogen oxidation reac-

tion and oxygen reduction reaction in the anode and cathode, respectively, creating and consuming protons.

#### 4.2 Species Transports

The present model takes into account two species in the anode ( $H_2$ ,  $H_2O$ ), and three in the cathode ( $O_2$ ,  $H_2O$ ,  $N_2$ ). The species transports based on the Stefan-Maxwell multi-component diffusion are given by the following equations

$$\rho u \cdot \nabla \omega_i = \nabla \cdot \left\{ \rho \omega_i \sum_{j=1}^N (1-S)^{1.5} D_{ij} \left[ \frac{M}{M_j} \left( \nabla \omega_j + \omega_j \frac{\nabla M}{M} \right) + (x_j - \omega_j) \frac{\nabla p}{p} \right] \right\} + S_s \quad (10)$$

where,  $\rho$  is the density,  $u$  is the velocity vector,  $p$  is the pressure,  $\omega$  is the molar fraction,  $M$  is the molar mass,  $x$  is the mass fraction, and  $D$  is the mass diffusivity.

The source term  $S_s$  is implemented based on electrochemical kinetics, i.e. consumption of the reactants to produce a current. It becomes  $S_s = j_{T,ca}(1-S)M_{O_2}/4F$  and  $j_{T,an}(1-S)M_{H_2}/2F$  in the cathodic and the anodic catalyst layers, respectively, and  $S$  represents the liquid water saturation.

#### 4.3 Momentum Transports

The Brinkman-extended Darcy equation, together with the mass conservation equation, describes the fluid flow in a porous media

$$\rho u \cdot \nabla u = -\nabla p + \nabla \cdot (\mu \nabla u) + S_m \quad (11)$$

$$\nabla(\rho u) = 0 \quad (12)$$

where,  $\mu$  is the viscosity, and the source term in the momentum equations is added based on Darcy's law, representing an extra drag force proportional to the fluid viscosity and velocity. It is inversely proportional to the permeability of a porous medium, i.e.  $S_m = -(\mu/\kappa)u$ , where  $\kappa$  is the permeability.

According to the Butler-Volmer equation [24], the relationships between the local transfer current density, the reactant concentrations, and the phase potentials can be described by the following equation

$$j_{T,ca} = j_{o,c} \left\{ \left( \frac{c_{O_2}}{c_{O_2,ref}} \right) \exp \left[ \frac{4a_c F}{RT} (\phi_m - \phi_s) \right] - \left( \frac{c_{H_2O}}{c_{H_2O,ref}} \right)^2 \times \exp \left[ \frac{4(1-a_c)F}{RT} (\phi_m - \phi_s) \right] \right\} \quad (13)$$

$$j_{T,an} = j_{o,a} \left\{ \left( \frac{c_{H_2O}}{c_{H_2O,ref}} \right)^2 \exp \left[ \frac{4a_a F}{RT} (\phi_s - \phi_m) \right] \right\} \quad (14)$$

where,  $j_{o,c}$  and  $j_{o,a}$  are the cathodic and anodic current exchange densities, respectively.



## 4.4 Conservation of Mass

The conservation of mass is applied to solve for the saturation of liquid water, as follows:

$$\nabla \cdot \left( \rho_l \left[ -D_c \nabla S + \frac{\mu_g \kappa_{rl}}{\mu_l \kappa_{rg}} u_g \right] \right) = S_{v \leftrightarrow l} + S_w \quad (15)$$

where, the capillary diffusion coefficient,  $D_c$ , is defined as

$$D_c = -\frac{\kappa_l}{\mu_l} \frac{dP_c}{dS} \quad (16)$$

and

$$\kappa_l = \kappa \kappa_{rl}, \quad \kappa_g = \kappa \kappa_{rg} \quad (17)$$

$$\kappa_{rl} = S^3 \quad (18)$$

$$\kappa_{rg} = (1 - S)^3 \quad (19)$$

$$P_c = \sigma \cos \theta_c \left( \frac{\varepsilon}{\kappa} \right)^{0.5} g(S) \quad (20)$$

where, the Leverette function expression is dependent on the contact angle, as follows [25]:

$$g(S) = \begin{cases} 1.417(1 - S) - 2.12(1 - S)^2 + 1.263(1 - S)^3 & \text{if } 0 \leq \theta_c < \pi/2 \\ 1.417S - 2.12S^2 + 1.263S^3 & \text{if } \pi/2 \leq \theta_c < \pi \end{cases} \quad (21)$$

The two source terms in the mass conservation equation of liquid water describe the condensation or evaporation of liquid water due to phase change from vapor to liquid, or *vice versa*, in the gas diffusion and catalyst layers, and the addition of liquid water *via* the electrochemical reaction, in the catalyst layer. The first source term,  $S_{v \leftrightarrow l}$ , can be described as

$$S_{v \leftrightarrow l} = \begin{bmatrix} \chi E \frac{M_{H_2O}}{RT} (x_{H_2O} p_g - p_{sat})(1 - S)f(S) + \\ E \frac{M_{H_2O}}{RT} S(x_{H_2O} p_g - p_{sat})(1 - f(S)) \end{bmatrix} \quad (22)$$

where,  $\chi$  is the condensation constant,  $E$  is the evaporation constant, and  $f(S)$  is the switch function, which is dependent on the RH inside the GDL and CL.

$$f(S) = \begin{cases} 0 & \text{if } \frac{x_{H_2O} p_g}{p_{sat}} \leq 1 \\ 1 & \text{if } \frac{x_{H_2O} p_g}{p_{sat}} > 1 \end{cases} \quad (23)$$

The production of water,  $S_w$ , can be expressed as  $S_w = j_{T,an}(1 - S)M_{H_2}/2F$ .

## 4.5 Convection and Conduction

A model of convection and conduction was developed to describe the thermal temperature distribution of the 3D PEM fuel cell. This model can be separated into three conduction parts (i.e. conduction of anode and cathode flow, the gas diffusion layer, and the membrane) and two convection parts (i.e. convection between flow and the gas diffusion layer and between the gas diffusion layer and the membrane).

The mathematical equation is as follows:

$$\nabla \cdot (-k \nabla T_1) = Q - \rho C_p u \nabla T_1, \quad (24)$$

where  $k$  is the thermal conductivity ( $W mK^{-1}$ ) of the flow part, GDL, and membrane.  $Q$  is the heated source at the electrode. A detailed representation of the CFD model is provided in a previous study [26]. Table 1 shows the electrochemical and physical properties used in the calculation.

## 5 Results of the CFD Analysis

The polarization curve was first obtained and compared to verify the accuracy of the CFD model; the result is shown in Figure 10. The excellent agreement between the experimental and CFD results is evident. The CFD model simultaneously utilized current, diffusion, and momentum equations to obtain polarization curves. Current flow, species flow, and

Table 1 Electrochemical properties of the modeled fuel cell.

Description	Value	References
Exchange current density ( $j_{o,a}$ )	$5 \times 10^3 [A m^{-2}]$	[28]
Exchange current density ( $j_{o,c}$ )	$5 \times 10^{-3} [A m^{-2}]$	[28]
Symmetric factor ( $a_a$ )	1.0	[28]
Symmetric factor ( $a_c$ )	0.5	[28]
GDL porosity ( $\varepsilon_{GDL}$ )	0.5	[27]
CL porosity ( $\varepsilon_{CL}$ )	0.4	[27]
Electrolyte fraction in CL ( $\varepsilon_m$ )	0.15	[27]
Solid fraction in CL ( $\varepsilon_s$ )	0.3	[27]
Permeability ( $\kappa$ )	$5.5 \times 10^{-11} [m^2]$	[27]
Electric conductivity ( $\sigma_s$ )	115 [ $S m^{-1}$ ]	[27]
Cathode inlet pressure ( $P_{a,in}$ )	[atm]	[27]
Anode inlet pressure ( $P_{c,in}$ )	[atm]	[27]
Operating temperature ( $T$ )	40 [ $^{\circ}C$ ]	[27]
Oxygen reference concentration ( $C_{O_2,ref}$ )	3.38 [ $mol m^{-3}$ ]	[27]
Order of reaction ( $\gamma_{O_2}$ )	1.0	[28]
Evaporation constant ( $E$ )	100 [ $s^{-1}$ ]	[27]
Condensation constant ( $\chi$ )	100 [ $s^{-1}$ ]	[27]
Pore size distribution ( $\delta$ )	7.2	[27]
Surface tension ( $\sigma$ )	0.062 [ $N m^{-1}$ ]	[27]
Contact angle ( $\theta_c$ )	100 [degree]	[27]

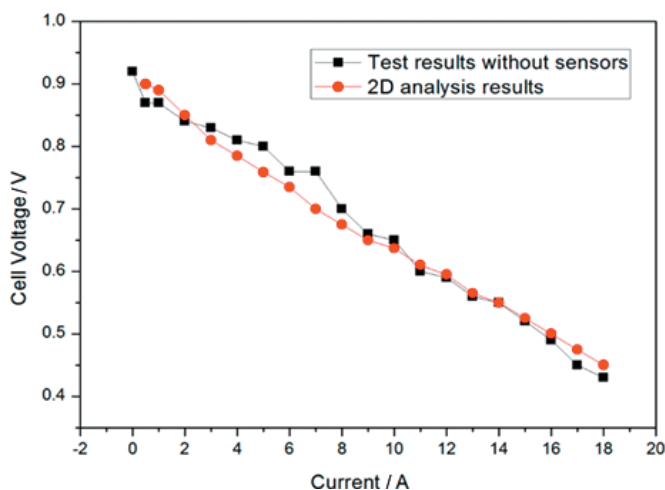


Fig. 10 Performance comparison between experiment and CFD results.

diffusion characteristics, as well as their pressure and velocity distribution, agree well with the experimental data. The conduction and convection partial differential equation was solved to obtain the temperature distribution. Figure 11 depicts the results of the temperature analysis at points 1, 2, and 3, with 8 A current. The cathode section shows a higher temperature than the anode one. Finally, the temperature at the three points was compared with the experimental results,

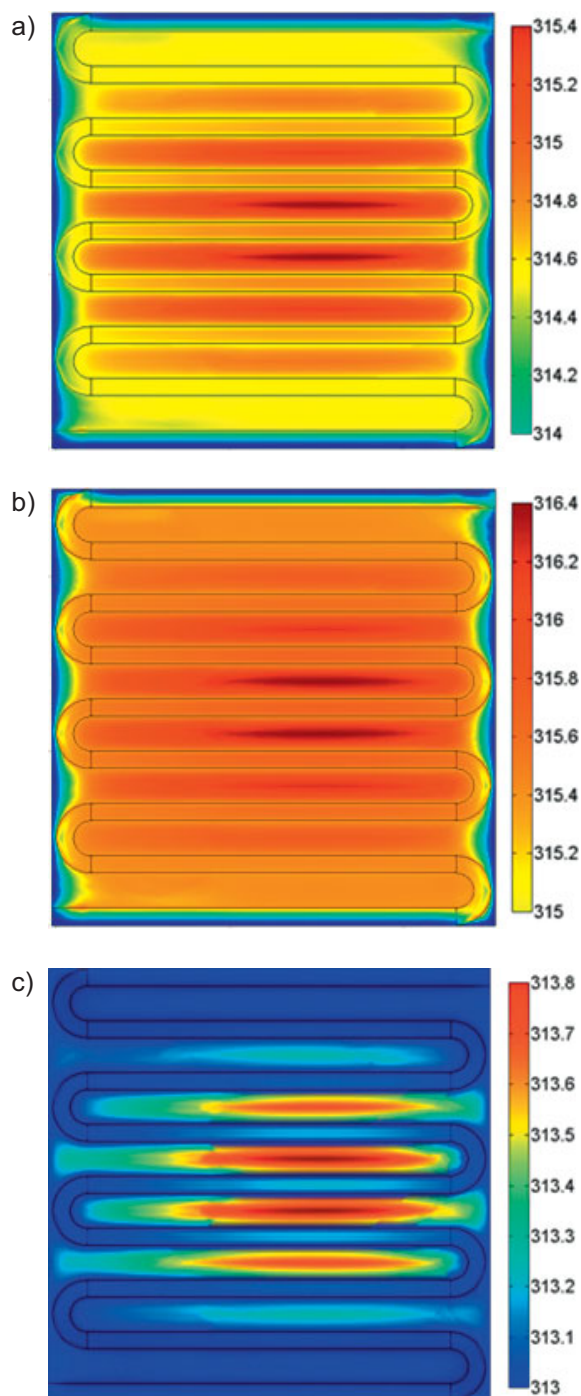


Fig. 11 Temperature distribution with current = 8 A: (a) point 1; (b) point 2; (c) point 3.

as presented in Figure 12. Excellent agreement between the CFD and experimental results was obtained and indirectly proved the accuracy of the CFD model.

## 6 Conclusion

A micro temperature sensor was successfully fabricated and utilized to measure the internal temperature of a fuel cell without a significant degradation in fuel cell performance. A flexible polyimide film was used as the substrate of the sensor, which can be placed anywhere to measure temperature. A programmable temperature chamber was used for sensor calibration to evaluate sensor properties; a unit fuel cell with an area of 25 cm<sup>2</sup> and a serpentine-type flow channel were utilized to examine the *in situ* sensor and determine how much it interrupted gas flow. A fuel cell polarization curve was obtained through a change in operating conditions, and the curve showed that the micro *in situ* sensor can be successfully utilized to measure fuel cell properties without a significant degradation in fuel cell performance. A 3D CFD model was developed and solved after the through-plane temperature distribution was obtained to numerically determine the temperature distribution. The CFD model showed excellent agreement with the experimental results in the polarization curve and temperature distribution. Overall, the findings of this study verify the modeling, diagnosis, monitoring, and control of the fuel cell to optimize its performance and extend its life expectancy.

## Acknowledgement

This research was supported by the National Research Foundation of Korea (NRF) funded by the Ministry of Education, Science and Technology (2013-005339).

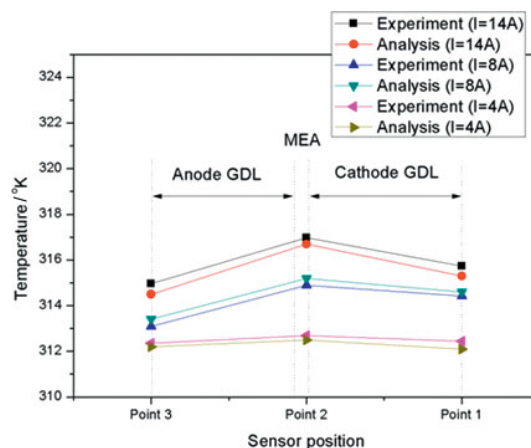


Fig. 12 Temperature comparison between experiment and CFD results (with RH = 60%).



## References

- [1] M. M. Mench, C. Y. Wang, M. Ishikawa, *J Electrochem. Soc.* **2003**, 150, A1052.
- [2] www.koreaittimes.com, May 4th, **2013**.
- [3] G. Hinds, M. Stevens, J. Wilkinson, M. de Podesta, S. Bell, *J. Power Sources* **2009**, 186, 52.
- [4] W. P. Partridge, T. J. Troops, J. B. Green, T. R. Armstrong, *J. Power Sources* **2006**, 160, 454.
- [5] Y. S. Chen, H. Peng, D. S. Hussey, D. L. Jacobson, D. T. Tran, T. Abdel-Baset, M. Biernacki, *J. Power Sources* **2007**, 170, 376.
- [6] M. M. Mench, Q. L. Dong, C. Y. Wang, *J. Power Sources* **2003**, 124, 90.
- [7] S. He, M. M. Mench, S. Tadigadapa, *Sens. Actuat. A* **2006**, 125, 170.
- [8] G. Zhang, L. Guo, L. Ma, H. Liu, *J. Power Sources* **2010**, 195, 3597.
- [9] C. Y. Lee, G. W. Wu, W. J. Hsieh, *J. Power Sources* **2007**, 172, 363.
- [10] C. Y. Lee, W. J. Hsieh, G. W. Wu, *J. Power Sources* **2008**, 181, 237.
- [11] Y. Shan, S. Y. Choe, *J. Power Sources* **2005**, 145, 30.
- [12] R. N. Methekar, V. Prasad, R. D. Gudi, *J. Power Sources* **2007**, 165, 152.
- [13] X. Xue, J. Tang, A. Smirnova, R. England, N. Sammers, *J. Power Sources* **2004**, 133, 188.
- [14] M. Khandelwal, S. Lee, M. M. Mench, *J. Power Sources* **2007**, 172, 816.
- [15] Y. X. Wang, Y. B. Kim, *IEEE/ASEM Mechatronics* **2014**, 19, 852.
- [16] H. Ju, H. Meng, C. Y. Meng, *Int. J. Heat Mass Transfer* **2005**, 48, 1303.
- [17] L. Matamoros, D. Brüggermann, *J. Power Sources* **2006**, 161, 203.
- [18] A. D. Manso, F. F. Marzo, M. Garmendia, J. Barranco, A. Lorenzo, *Int. J. Hydrogen Energy* **2011**, 36, 6795.
- [19] W. J. Yang, S. J. Kang, Y. B. Kim, *Int. J. Energy Res.* **2012**, 36, 1051.
- [20] J. G. Pharoah, O. S. Burheim, *J. Power Sources* **2010**, 195, 5235.
- [21] W. Y. Chang, T. H. Fang, Y. C. Lin, *Appl. Phys. A* **2008**, 92, 693.
- [22] W. J. Yang, H. Y. Wang, Y. B. Kim, *Int. J. Energy Res.* **2013**, 37, 1339.
- [23] J. J. Hwang, *J. Electrochem. Soc.* **2006**, 153, 216.
- [24] J. J. Hwang, *J. Power Sources* **2007**, 164, 174.
- [25] P. Costamagna, K. Honegger, *J. Electrochem. Soc.* **1998**, 145, A3995.
- [26] Y. B. Kim, *Int. J. Energy Res.* **2012**, 36, 509.
- [27] N. Zamel, X. Li, *Int. J. Energy Res.* **2008**, 32, 698.
- [28] M. Amirinejad, S. Rowshanzair, M. H. Eikani, *J. Power Sources* **2006**, 161, 872.